# Synaptic vesicle glycoprotein 2A is affected in the CNS of Huntington's disease mice and *post-mortem* human HD brain

Daniele Bertoglio[1], Jeroen Verhaeghe[1], Leonie wyffels[1,2], Alan Miranda[1], Sigrid Stroobants[1,2], Ladislav Mrzljak[3], Celia Dominguez[3], Mette Skinbjerg[3], Jonathan Bard[3], Longbin Liu[3], Ignacio Munoz-Sanjuan[3], Steven Staelens[1]

[1]Molecular Imaging Center Antwerp (MICA), University of Antwerp, Wilrijk, Belgium

[2]Department of Nuclear Medicine, Antwerp University Hospital, Edegem, Belgium

[3]CHDI Management/CHDI Foundation, Los Angeles, California, USA


**Corresponding author:**

Prof. Steven Staelens

MICA, University of Antwerp, Universiteitsplein 1, Wilrijk, Belgium

Tel. +32 032652820; Email: steven.staelens@uantwerpen.be


Daniele Bertoglio, PhD

MICA, University of Antwerp, Universiteitsplein 1, Wilrijk, Belgium

Tel. +32 032652816; Email: daniele.bertoglio@uantwerpen.be

Orcid: https://orcid.org/0000-0003-4205-5432

2

**Word count:** 4978 words

**Running title:** Preclinical SV2A PET imaging in HD

3

# ABSTRACT

Synaptic dysfunction is a primary mechanism underlying Huntington's Disease (HD) progression. This study investigated changes in synaptic vesicle glycoprotein 2A (SV2A) density by means of ^{11}C-UCB-J microPET imaging in the central nervous system (CNS) of HD mice.

**METHODS:** Dynamic ^{11}C-UCB-J microPET imaging was performed at clinically relevant disease stages (at 3, 7, 10, and 16 months, M) in the heterozygous knock-in Q175DN mouse model of HD and WT littermates ($n$=16-18/genotype and time point). Cerebral ^{11}C-UCB-J analyses were performed to assess genotypic differences during pre-symptomatic (3M) and symptomatic (7-16M) disease stages. ^{11}C-UCB-J binding in the spinal cord was quantified at 16M. ^{3}H-UCB-J autoradiography and SV2A immunofluorescence were performed *post-mortem* in mouse and human brain tissue.

**RESULTS:** ^{11}C-UCB-J binding was declined in symptomatic heterozygous mice compared to WT littermates in parallel with disease progression (7M: $p<0.01$, 16M: $p<0.0001$). Specific ^{11}C-UCB-J binding was detectable in the spinal cord, with symptomatic heterozygous mice displaying a significant reduction ($p<0.0001$). ^{3}H-UCB-J autoradiography and SV2A immunofluorescence corroborated the *in vivo* measurements demonstrating lowered SV2A in heterozygous mice ($p<0.05$). Finally, preliminary analysis of SV2A in *post-mortem* human brain suggested lower SV2A in HD gene carrier compared to nondemented control.

**CONCLUSION:** ^{11}C-UCB-J PET detects SV2A deficits during symptomatic disease in heterozygous mice in both brain and spinal cord, offering a novel marker of synaptic integrity widely distributed in CNS. Upon clinical application, ^{11}C-UCB-J PET imaging yields promise for SV2A measurement in patients with HD during disease progression and following disease-modifying therapeutic strategies.

**Keywords:** SV2A; ^{11}C-UCB-J; spinal cord, Huntington's Disease; animal model

4

**INTRODUCTION**

Huntington's Disease (HD) is an autosomal dominant neurodegenerative disorder caused by an expanded polyglutamine repeat in exon 1 of the gene encoding the huntingtin protein (*1*), which leads to the expression of mutated huntingtin (mHTT). Pathological features of HD include wide-spread progressive accumulation of mHTT, selective neurodegeneration, and forebrain atrophy (*2,3*).

A growing body of evidence suggests that mHTT induces synaptic transmission dysfunction (*4*), thus synaptic dysfunction represents one of the main mechanisms underlying the progression of HD (*5*). Alterations in pre-synaptic proteins, including regulators of endocytosis and exocytosis of synaptic vesicles such as synaptosome-associated protein 25 and rabphilin 3A have been reported in both clinical (*6,7*) and preclinical (*8-10*) *post-mortem* studies. Previous studies have demonstrated mHTT abnormally associates with synaptic vesicles resulting in impaired synaptic function (*11*) and changes in synaptic proteins correlate with behavioural deficits (*10*), Thus, alterations in synaptic proteins may represent a candidate marker to monitor HD progression (*12-14*). Given the current lack of effective treatment to prevent the disease or halt its progression, synaptic markers may play an important role in the development and evaluation of novel disease-modifying therapies throughout the entire central nervous system (CNS) (*15*).

Among pre-synaptic proteins, the synaptic vesicle glycoprotein 2A (SV2A) is an essential vesicle membrane protein involved in neurotransmitter release and is expressed ubiquitously in synapses of the brain (*16,17*). Recent studies have reported that SV2A can be imaged non-invasively in non-human primates, humans, and rodents utilizing positron emission tomography (PET) with the selective and high-affinity radioligand ^{11}C-UCB-J (*18-20*). ^{11}C-UCB-J PET may offer a proxy to assess synaptic density *in vivo* given its optimal clinical and preclinical pharmacokinetics and quantification properties (*20,21*). Thus, it provides a quantitative measure of the synaptic changes during HD progression.

5

Here, for the first time, we investigated ^{11}C-UCB-J PET imaging to quantify cerebral SV2A levels at clinically relevant disease stages in the knock-in Q175DN mouse model for HD (*22-24*). Additionally, given the evidence of mHTT pathology in the spinal cord (*25*), we evaluated the use of ^{11}C-UCB-J PET imaging to detect SV2A density changes in the rodent cervical spinal cord. Finally, *post-mortem* measurements of SV2A were performed in the mouse as well as in a preliminary exploratory evaluation in the human brain.

## MATERIAL AND METHODS

### Animals

Male wild-type (WT, *n* = 35) mice and age-matched heterozygous knock-in Q175DN littermates (*n* = 35) (C57BL/6J background, CHDI-81003019) were obtained from Jackson Laboratories (Bar Harbour, Maine, USA). The animals were single-housed in individually ventilated cages under a 12h light/dark cycle in a temperature- and humidity-controlled environment with food and water *ad libitum* with at least one week to acclimatize. All experiments were approved by the Ethical Committee for Animal Testing (ECD 2017-27) at the University of Antwerp (Belgium), the European Committee Guidelines (decree 2010/63/CEE).

The Q175DN model displays a moderately slow disease progression with the hallmark of mHTT accumulation increasing from 3 to 12 months (M) (*26*). This animal model features motor deficits appearing around 6M followed by cognitive decline around 10M (*22,27*). Thus ^{11}C-UCB-J PET imaging was performed at clinically relevant disease stages: cross-sectional at 3M (pre-symptomatic stage, *n*=16/genotype); longitudinal at 7, 10, and 16M (appearance, progression, and advanced symptomatic stages, respectively, *n*=19/genotype).

6

**Tracer Radiosynthesis**

[11]C-UCB-J synthesis was performed on an automated synthesis module (Carbosynthon I, Comecer, The Netherlands) adapting the previously described procedure (*18*) to our system (*20*). Average radiochemical purity was greater than 99%, and molar activity was 96.5 ± 13.3 GBq/µmol.

**[11]C-UCB-J Dynamic MicroPET Scan**

MicroPET/Computed tomography (CT) imaging was performed on two Siemens Inveon PET/CT scanners (Siemens Preclinical Solution, USA). Animal preparation was performed as previously described (*20*). At the start of the dynamic microPET scan, animals were injected via the tail vein with a bolus of ^{11}C-UCB-J (5.4 ± 1.3 MBq) over a 12-second interval (1 ml/min) using an automated pump (Pump 11 Elite, Harvard Apparatus, USA). The activity was injected in a trace dose keeping the cold mass within 2.0 µg/kg across time points for consistency. Data were acquired in list-mode format. Following the microPET scan, a 10 min 80 kV/500 µA CT scan was performed for co-registration and attenuation correction. Detailed information on the scan parameters is reported in Supplemental Table 1. Published work from our group (*20*) was re-analyzed for blocking validation of ^{11}C-UCB-J binding in the spinal cord. Blocking was achieved by pre-treatment with levetiracetam at either 50 (*n* = 4) or 200 (*n* = 4) mg/kg, injected intraperitoneally 30 min before radioligand delivery. Representative SUV images were generated based on the interval 10-90 min.

**Image Processing and Analysis**

Acquired PET data were histogrammed and reconstructed into 33 frames of increasing length (12x10s, 3x20s, 3x30s, 3x60s, 3x150s, and 9x300s). For quantitative

7

analysis, all images were reconstructed using a list-mode iterative reconstruction with spatially variant resolution modeling with 8 iterations and 16 subsets of the 3D ordered subset expectation maximization (OSEM-3D) algorithm (*28*). Normalization, dead time, and CT-based attenuation corrections were applied. PET image frames were reconstructed on a 128x128x159 grid with 0.776x0.776x0.796 mm$^3$ voxels. PET images were processed and analyzed using PMOD 3.6 software (Pmod Technologies, Zurich, Switzerland).

Spatial normalization of the PET images was done through brain normalization of the PET images to an ^{11}C-UCB-J PET template as we previously described (*20*). Using the volume-of-interest template based on the Waxholm atlas (*29*), time-activity curves of different regions (striatum, motor cortex, hippocampus, and thalamus) were extracted from the images. Cervical spinal cord volume-of-interest was manually delineated on the individual CT images (blinded to condition) and time-activity curves were extracted. Kinetic modeling was performed to fit the time-activity curves by a standard one-tissue compartmental model (1TCM) to determine the total volume of distribution using a non-invasive image-derived input function (IDIF) to calculate $V_{T\ (IDIF)}$ as a surrogate of $V_T$ estimate as we recently validated (*20*). No genotypic difference in plasma-to-whole blood ratio or plasma radiometabolites was present between genotypes, therefore no correction was applied (*20*).

Parametric $V_{T\ (IDIF)}$, as well as $K_1$ maps, were generated in PMOD through voxel-wise analysis (1TCM) (*20*). Brain parametric maps are represented as averages for each genotype overlaid on a 3D mouse brain MR template for anatomical reference, while maps focusing on the spinal cord are represented as individual animal overlaid on CT.

**Mouse Brain Tissue**

Upon termination of the longitudinal study, 16M animals (WT, *n*=16; heterozygous,

*n*=13) were euthanized by decapitation while anesthetized, brains were snap-frozen in 2-metylbuthane at -35°C for 2 min and preserved at -80°C until use. Serial sagittal sections (20 µm of thickness) were collected starting at 1.80 mm lateral bregma (*30*) in triplicate on Superfrost Plus slides (Thermo Fischer Scientific, USA), using a cryostat (Leica, Germany)

### *Post-mortem* Human Brain Tissue

Fresh-frozen *post-mortem* superior frontal gyrus tissue was obtained from The Netherlands Brain Bank (NBB), Netherlands Institute for Neuroscience, Amsterdam (open access: www.brainbank.nl). All Material has been collected from donors for or from whom a written informed consent for a brain autopsy and the use of the material and clinical information for research purposes had been obtained by the NBB. Ethical permission for the study was obtained from the Committee for Medical Ethics of the University of Antwerp/University Hospital Antwerp (20/13/155).

Tissue was obtained from female donors (age range: 50-67 years) with a *post-mortem* interval (PMI) less than 8 h for all cases. Since SV2A has been reported to be decreased in patients with Alzheimer's disease *(31)*, tissue was assessed for evidence of neurological morbidities (beta-amyloid and tauopathy) through immunostaining. After exclusion of nondemented controls and symptomatic HD carriers positive to beta-amyloid aggregates and/or tau tangles, only one nondemented control (ID 2017-005, Female, 60 years, PMI = 5.5 h) and one symptomatic HD gene carrier (ID 2017-060, Female, 57 years, PMI = 6.7 h) were included in the investigation. Although the CAG repeat length for HD subjects was not available in the NBB database, the presence of mHTT aggregates was confirmed histologically. Serial sections (10 µm of thickness) were collected on Superfrost Plus slides (Thermo Fischer Scientific, USA), using a cryostat (Leica, Germany).

9

**Autoradiography**

$^3$H-UCB-J autoradiography was performed in mice at 16M as well as on *post-mortem* human tissue as we previously described (*32*) following validation of SV2A selectivity using a blocking solution (1 nM of $^3$H-UCB-J + 1 mM of levetiracetam in binding buffer) to validate $^3$H-UCB-J specificity towards SV2A (Supplemental Figure 1). $^3$H-UCB-J was synthesized at Pharmaron (UK) with molar radioactivity of 1295 MBq/μmol and radiochemical purity >99%.

Regional quantification was performed blind to genotype using Fiji software (National Institute of Health, USA). $^3$H-UCB-J binding was measured in triplicate (3 slices) manually drawn the regions. Regional specific binding of $^3$H-UCB-J was measured by converting the mean grey values into radioactivity density (Bq/mg) calculated using commercial tritium standards (American Radiolabeled Chemicals). Next, using $^3$H-UCB-J molar activity on the experimental day, radioactivity density was converted into binding density (fmol/mg) for each region.

**Immunofluorescence**

SV2A immunofluorescence was performed in mice at 16M as well as on *post-mortem* human tissue. Sections were air-dried for 5 min and incubated with 4% paraformaldehyde for 15 min as tissue post-fixation. Next, slices were rinsed using phosphate-buffered saline (PBS) and non-specific binding sites were blocked using 20% normal donkey serum (NDS) in PBS for 1 h. Then, sections were incubated with the primary antibody anti-SV2A (rabbit anti-mouse; 1:400; #66724, Cell signalling technologies) in antibody diluent containing 5% NDS in PBS overnight at room temperature. The next day, sections were washed with PBS prior to being incubated for 1 h with secondary donkey anti-rabbit (1:100; Alexa Fluor 488, Jackson ImmunoResearch) in antibody diluent containing 5% NDS in PBS. Following washes with PBS, sections were

10

mounted with 4′,6-diamidino-2-phenylindol (DAPI, Vector Laboratories), and coverslipped. Images at 20X and 100X magnification were acquired for quantification with a high throughput fluorescence microscope (Nikon, Japan) with NIS elements software.

Quantification was performed blind to genotype using Fiji software. Since the white matter was devoid of a specific signal, after conversion into 8-bit grayscale, an intensity threshold was set to remove the background signal in the white matter (threshold 27 out of 255) and convert images into binary data. Regions-of-interest (striatum, motor cortex, hippocampus, and thalamus for mouse; a cortical grey matter for human tissue) were manually drawn on each image, and the percentage of surface area after thresholding was measured as the positive area. Quantification was done in triplicate (3 slices) for each region and the average was used for statistical analysis.

**Statistical Analysis**

All data were normally distributed as assessed using the Shapiro-Wilk test. Longitudinal PET data were analyzed with a linear mixed-model by fitting each region separately using $^{11}$C-UCB-J $V_{T\,(IDIF)}$ or $K_{1\,(IDIF)}$ as dependent variables, while genotype (WT and heterozygous), time (7, 10, and 16M), and the interaction between genotype and time (genotype*time) as fixed effects, with subjects as a random effect. The comparison was performed to evaluate regional temporal and genotypic differences. Two-way ANOVA (genotype and region as variables) was applied to investigate the 3M data and *post-mortem* analyses. One-way ANOVA was used for blocking analysis in the spinal cord, while an unpaired T-test was used to compare the genotypic difference in spinal cord SV2A PET. Pearson's correlation test was used to determine the relationship between variables. Normality and two-way ANOVA tests were performed with GraphPad Prism (v 9.0) statistical software, linear mixed-model in JMP Pro 13 (SAS), and calculation of the effect size *d* with G*Power software (http://www.gpower.hhu.de/). *P* values were corrected

11

for multiple comparisons using the Tukey's test. Data are represented as mean ± standard deviation (SD). All tests were two-tailed and statistical significance was set at $p<0.05$.

## RESULTS

### SV2A Density Decreases with HD Progression

Longitudinal mean $V_{T\ (IDIF)}$ parametric maps of ^{11}C-UCB-J at 7, 10, and 16M, displayed a broad cerebral reduction of ^{11}C-UCB-J binding in symptomatic heterozygous mice compared to WT littermates (Figure 1A). Accordingly, ^{11}C-UCB-J $V_{T\ (IDIF)}$ values were significantly reduced in heterozygous mice compared WT animals at all stages of disease investigated (namely 7, 10, and 16M) in parallel with HD progression (e.g. striatum: -13.4±3.4%, $p<0.01$; -10.8±4.0%, $p<0.01$; -20.3±4.0%, $p<0.0001$ at 7, 10, and 16M, respectively) (Figure 1B and Supplemental Table 2). Notably, the reduced ^{11}C-UCB-J uptake was not related to altered $K_1$ values (delivery rate of the tracer; Supplemental Figure 2), suggesting the reduced binding was not reflecting a mere decrease in cerebral perfusion.

No difference in ^{11}C-UCB-J $V_{T\ (IDIF)}$ values between WT and pre-symptomatic heterozygous mice (3M) was observed ($F_{(1,116)}=2.847$, $p=0.092$; e.g. striatum: -3.1±4.1%) (Figure 2). $V_{T\ (IDIF)}$ values at different ages are reported in Supplemental Table 3.

### SV2A Levels Are Reduced in the Spinal Cord of Symptomatic Heterozygous Mice

We explored the potential application of ^{11}C-UCB-J PET to detect SV2A in the mouse spinal cord. ^{11}C-UCB-J binding quantifiable and specific as validated following pre-treatment with levetiracetam ($F_{(2,10)}=78.96$, $p<0.0001$) (Figure 3).

12

Next, based on clinical evidence indicating the presence of mHTT pathology in the spinal cord, we quantified ^{11}C-UCB-J PET in the mouse cervical spinal cord of symptomatic heterozygous mice (16M). As shown in Figure 4, ^{11}C-UCB-J binding was significantly reduced in the cervical spinal cord of heterozygous mice compared to WT littermates (-22.5±3.8%, $p<0.0001$) (Figure 4B) with a strong association to the cortical quantification ($r^2=0.90$, $p<0.0001$) (Figure 4C).

### *Post-mortem* Rodent and Human Studies Corroborate SV2A Reduction in HD

[3]H-UCB-J specific binding was significantly reduced in heterozygous mice compared to WT littermates ($F_{(1,104)}=35.77$, $p<0.0001$; e.g. striatum: -22.1±8.3%); in agreement with the *in vivo* measurement and corroborated by SV2A immunostaining ($F_{(1,104)}=51.42$, $p<0.0001$; e.g. striatum: -12.0±4.5%) (Figure 5A).

We performed a preliminary assessment of ^{3}H-UCB-J binding in the *post-mortem* human cortex of control and an HD gene carrier (Figure 5B). Both ^{3}H-UCB-J specific binding and SV2A immunostaining indicated a lower SV2A signal in the HD gene carrier (Figure 5C).

## DISCUSSION

This work assessed synaptic integrity using the PET radioligand ^{11}C-UCB-J in heterozygous mice at clinically relevant pre- and symptomatic stages of the disease. This work represents the first evidence of *in vivo* changes in SV2A density. In particular, changes in synaptic density were detectable at all symptomatic stages of HD with mHTT accumulation broadly affecting SV2A levels in the entire CNS.

Despite the mounting evidence indicating mHTT induces pre-synaptic transmission dysfunction during the progression of HD (*4,5*), to date no clinical or

13

preclinical studies have assessed alterations in presynaptic proteins *in vivo*. Nonetheless, cross-sectional findings in animal models of HD suggested a reduction in different synaptic proteins in different animal models at symptomatic but not pre-symptomatic stages of the disease (*8-10*), in agreement with our observation *in vivo* in heterozygous mice as well as *in vitro* in both HD mice and *post-mortem* human tissue.

Since the development of SV2A radioligands for *in vivo* imaging of SV2A (*18,19*), preclinical and clinical investigations have been restricted on the brain despite SV2A is distributed in all grey matter, including the spinal cord (*33*). Thus, we evaluated the specificity of the ^{11}C-UCB-J signal in the cortical spinal cord using our previous levetiracetam blocking study (*20*), demonstrating, for the first time, the capability of SV2A PET imaging in the spinal cord of a living animal. Interestingly, Lanberg and colleagues reported a 2-to-3-fold difference in SV2A expression in the spinal cord compared to the cerebral cortex in the rat (*33*). In this work, we measured a 2.5-fold difference in ^{11}C-UCB-J binding between the spinal cord and motor cortex, in agreement with the previous rat report (*33*). Next, based on the clinical evidence of mHTT pathology in the spinal cord (*25*), we explored ^{11}C-UCB-J binding in the cervical spinal cord of symptomatic heterozygous mice and observed a decline in SV2A density with a similar magnitude to the brain. Altogether these observations support the exploration of SV2A PET imaging as synaptic integrity marker in spinal cord-related disorders, for instance, amyotrophic lateral sclerosis as well as spinal cord injury (SCI), currently being investigated in our group and supported by the recent evidence that levetiracetam treatment leads to functional recovery in SCI models (*34*).

In recent years, the field of PET imaging has significantly progressed in the identification of different striatal markers to monitor HD progression (*35-41*). However, since the whole CNS is affected in HD, non-invasive markers with ubiquitous brain distribution such as ^{11}C-UCB-J PET imaging may provide unique insights in elucidating

global pathophysiological changes during HD. Intriguingly, clinical feasibility in detecting SV2A decline  has been reported in other neurodegenerative disorders, including Alzheimer's disease and Parkinson's disease (*31,42*).

**CONCLUSION**

Collectively, these findings demonstrate significant SV2A deficits in the brain and spinal cord of symptomatic heterozygous mice. ^{11}C-UCB-J PET imaging is a promising marker for the assessment of synaptic integrity in patients with HD during disease progression and following disease-modifying therapeutic strategies.

15

**DISCLOSURE**

**ACKNOWLEDGEMENTS**

**KEY POINTS**

**Question:**

Is SV2A density affected during the progression of Huntington's Disease (HD)?

**Pertinent findings:**

In this ^{11}C-UCB-J positron emission tomography (PET) study, we demonstrated brain and spinal cord SV2A deficits during symptomatic disease in HD mice i, highlighting the potential of SV2A PET as a marker in the entire central nervous system (CNS).

**Implication for patient care:**

[11]C-UCB-J PET imaging offers a unique tool as CNS functional marker for HD, and yields promising application for SV2A measurement in patients with HD during disease progression and following therapeutic interventions.

## REFERENCES

**1.** The Huntington's Disease Collaborative Research Group. A novel gene containing a trinucleotide repeat that is expanded and unstable on Huntington's disease chromosomes. *Cell.* 1993:971-983.

**2.** Rub U, Vonsattel JP, Heinsen H, Korf HW. The Neuropathology of Huntington s disease: classical findings, recent developments and correlation to functional neuroanatomy. *Adv Anat Embryol Cell Biol.* 2015;217:1-146.

**3.** Waldvogel HJ, Kim EH, Tippett LJ, Vonsattel JP, Faull RL. The neuropathology of Huntington's disease. *Curr Top Behav Neurosci.* 2015;22:33-80.

**4.** Rozas JL, Gomez-Sanchez L, Tomas-Zapico C, Lucas JJ, Fernandez-Chacon R. Presynaptic dysfunction in Huntington's disease. *Biochem Soc Trans.* 2010;38:488-492.

**5.** Sepers MD, Raymond LA. Mechanisms of synaptic dysfunction and excitotoxicity in Huntington's disease. *Drug Discov Today.* 2014;19:990-996.

**6.** Smith R, Klein P, Koc-Schmitz Y, et al. Loss of SNAP-25 and rabphilin 3a in sensory-motor cortex in Huntington's disease. *J Neurochem.* 2007;103:115-123.

**7.** Fourie C, Kim E, Waldvogel H, et al. Differential Changes in Postsynaptic Density Proteins in Postmortem Huntington's Disease and Parkinson's Disease Human Brains. *J Neurodegener Dis.* 2014;2014:938530.

**8.** Smith R, Petersen A, Bates GP, Brundin P, Li JY. Depletion of rabphilin 3A in a transgenic mouse model (R6/1) of Huntington's disease, a possible culprit in synaptic dysfunction. *Neurobiol Dis.* 2005;20:673-684.

**9.** Shirendeb UP, Calkins MJ, Manczak M, et al. Mutant huntingtin's interaction with mitochondrial protein Drp1 impairs mitochondrial biogenesis and causes defective axonal transport and synaptic degeneration in Huntington's disease. *Hum Mol Genet.* 2012;21:406-420.

**10.** Smith GA, Rocha EM, McLean JR, et al. Progressive axonal transport and synaptic protein changes correlate with behavioral and neuropathological abnormalities in the heterozygous Q175 KI mouse model of Huntington's disease. *Hum Mol Genet.* 2014;23:4510-4527.

**11.** Li H, Wyman T, Yu ZX, Li SH, Li XJ. Abnormal association of mutant huntingtin with synaptic vesicles inhibits glutamate release. *Hum Mol Genet.* 2003;12:2021-2030.

**12.** Milnerwood AJ, Gladding CM, Pouladi MA, et al. Early increase in extrasynaptic NMDA receptor signaling and expression contributes to phenotype onset in Huntington's disease mice. *Neuron.* 2010;65:178-190.

**13.** DiProspero NA, Chen EY, Charles V, Plomann M, Kordower JH, Tagle DA. Early changes in Huntington's disease patient brains involve alterations in cytoskeletal and synaptic elements. *J Neurocytol.* 2004;33:517-533.

**14.** Milnerwood AJ, Raymond LA. Early synaptic pathophysiology in neurodegeneration: insights from Huntington's disease. *Trends Neurosci.* 2010;33:513-523.

**15.** Tabrizi SJ, Ghosh R, Leavitt BR. Huntingtin Lowering Strategies for Disease Modification in Huntington's Disease. *Neuron.* 2019;101:801-819.

**16.** Bajjalieh SM, Frantz GD, Weimann JM, McConnell SK, Scheller RH. Differential expression of synaptic vesicle protein 2 (SV2) isoforms. *J Neurosci.* 1994;14:5223-5235.

**17.** Janz R, Sudhof TC. SV2C is a synaptic vesicle protein with an unusually restricted localization: anatomy of a synaptic vesicle protein family. *Neuroscience.* 1999;94:1279-1290.

**18.** Nabulsi NB, Mercier J, Holden D, et al. Synthesis and Preclinical Evaluation of 11C-UCB-J as a PET Tracer for Imaging the Synaptic Vesicle Glycoprotein 2A in the Brain. *J Nucl Med.* 2016;57:777-784.

**19.** Finnema SJ, Nabulsi NB, Eid T, et al. Imaging synaptic density in the living human brain. *Sci Transl Med.* 2016;8:348ra396.

**20.** Bertoglio D, Verhaeghe J, Miranda A, et al. Validation and noninvasive kinetic modeling of [(11)C]UCB-J PET imaging in mice. *J Cereb Blood Flow Metab.* 2020;40:1351-1362.

**21.** Finnema SJ, Nabulsi NB, Mercier J, et al. Kinetic evaluation and test-retest reproducibility of [(11)C]UCB-J, a novel radioligand for positron emission tomography imaging of synaptic vesicle glycoprotein 2A in humans. *J Cereb Blood Flow Metab.* 2017:271678X17724947.

**22.** Menalled LB, Kudwa AE, Miller S, et al. Comprehensive behavioral and molecular characterization of a new knock-in mouse model of Huntington's disease: zQ175. *PLoS One.* 2012;7:e49838.

**23.** Heikkinen T, Lehtimaki K, Vartiainen N, et al. Characterization of neurophysiological and behavioral changes, MRI brain volumetry and 1H MRS in zQ175 knock-in mouse model of Huntington's disease. *PLoS One.* 2012;7:e50717.

19

**24.** Peng Q, Wu B, Jiang M, et al. Characterization of Behavioral, Neuropathological, Brain Metabolic and Key Molecular Changes in zQ175 Knock-In Mouse Model of Huntington's Disease. *PLoS One.* 2016;11:e0148839.

**25.** Sciacca G, Cicchetti F. Mutant huntingtin protein expression and blood-spinal cord barrier dysfunction in huntington disease. *Ann Neurol.* 2017;82:981-994.

**26.** Carty N, Berson N, Tillack K, et al. Characterization of HTT inclusion size, location, and timing in the zQ175 mouse model of Huntington's disease: an in vivo high-content imaging study. *PLoS One.* 2015;10:e0123527.

**27.** Heikkinen T, Bragge T, Bhattarai N, et al. Rapid and robust patterns of spontaneous locomotor deficits in mouse models of Huntington's disease. *PLoS One.* 2020;15:e0243052.

**28.** Miranda A, Bertoglio D, Glorie D, Stroobants S, Staelens S, Verhaeghe J. Validation of a spatially variant resolution model for small animal brain PET studies. *Biomed Phys Eng Expr.* 2020;6.

**29.** Johnson GA, Badea A, Brandenburg J, et al. Waxholm space: an image-based reference for coordinating mouse brain research. *Neuroimage.* 2010;53:365-372.

**30.** Paxinos G, Franklin K. *The mouse brain in stereotaxic coordinates*: Academic Press; 2 edition (December 8, 2003); 2003.

**31.** Chen MK, Mecca AP, Naganawa M, et al. Assessing Synaptic Density in Alzheimer Disease With Synaptic Vesicle Glycoprotein 2A Positron Emission Tomographic Imaging. *JAMA Neurol.* 2018;75:1215-1224.

**32.** Glorie D, Verhaeghe J, Miranda A, De Lombaerde S, Stroobants S, Staelens S. Sapap3 deletion causes dynamic synaptic density abnormalities: a longitudinal [(11)C]UCB-J PET study in a model of obsessive-compulsive disorder-like behaviour. *EJNMMI Res.* 2020;10:140.

**33.** Lambeng N, Gillard M, Vertongen P, Fuks B, Chatelain P. Characterization of [(3)H]ucb 30889 binding to synaptic vesicle protein 2A in the rat spinal cord. *Eur J Pharmacol.* 2005;520:70-76.

**34.** Lima R, Gomes ED, Cibrao JR, et al. Levetiracetam treatment leads to functional recovery after thoracic or cervical injuries of the spinal cord. *NPJ Regen Med.* 2021;6:11.

**35.** Haggkvist J, Toth M, Tari L, et al. Longitudinal microPET imaging of the zQ175 mouse model of Huntington's disease shows in vivo changes of molecular targets in the striatum and the cerebral cortex. *J Nucl Med.* 2016.

**36.**     Bertoglio D, Kosten L, Verhaeghe J, et al. Longitudinal characterization of mGluR5 using (11)C-ABP688 PET imaging in the Q175 mouse model of Huntington's disease. *J Nucl Med.* 2018.

**37.**     Bertoglio D, Verhaeghe J, Kosten L, et al. MR-based spatial normalization improves [18F]MNI-659 PET regional quantification and detectability of disease effect in the Q175 mouse model of Huntington's disease. *PLoS One.* 2018;13:e0206613.

**38.**     Russell DS, Barret O, Jennings DL, et al. The phosphodiesterase 10 positron emission tomography tracer, [18F]MNI-659, as a novel biomarker for early Huntington disease. *JAMA Neurol.* 2014;71:1520-1528.

**39.**     Pavese N, Andrews TC, Brooks DJ, et al. Progressive striatal and cortical dopamine receptor dysfunction in Huntington's disease: a PET study. *Brain.* 2003;126:1127-1135.

**40.**     Russell DS, Jennings DL, Barret O, et al. Change in PDE10 across early Huntington disease assessed by [18F]MNI-659 and PET imaging. *Neurology.* 2016;86:748-754.

**41.**     Bertoglio D, Kosten L, Verhaeghe J, et al. Longitudinal Characterization of mGluR5 Using (11)C-ABP688 PET Imaging in the Q175 Mouse Model of Huntington Disease. *J Nucl Med.* 2018;59:1722-1727.

**42.**     Matuskey D, Tinaz S, Wilcox KC, et al. Synaptic Changes in Parkinson Disease Assessed with in vivo Imaging. *Ann Neurol.* 2020;87:329-338.

**FIGURES WITH LEGENDS**
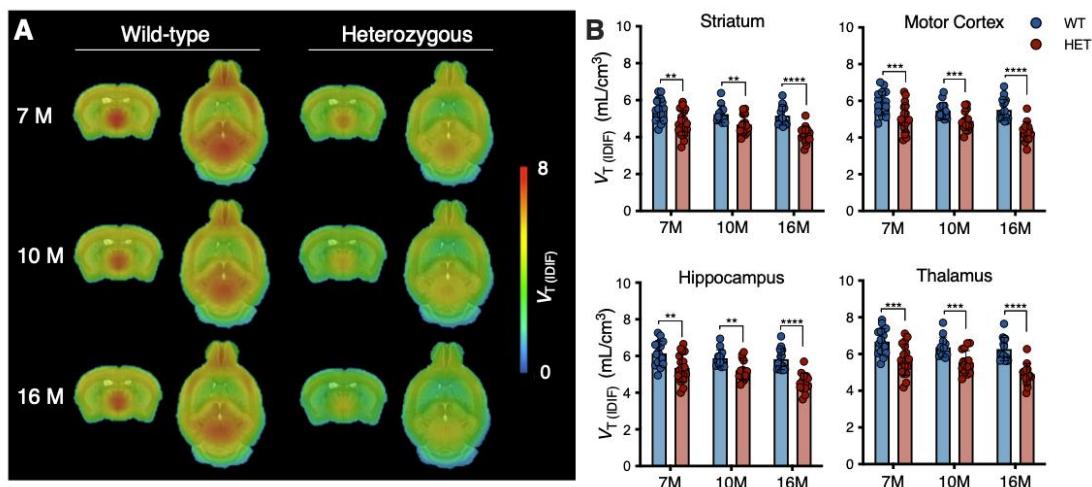


**FIGURE 1. $^{11}$C-UCB-J binding is reduced in symptomatic heterozygous mice.** (**A**) Mean parametric $^{11}$C-UCB-J $V_{T\,(IDIF)}$ maps of 7-, 10-, and 16-month old mice overlaid on MRI template for anatomical localization. (**B**) Cerebral $V_{T\,(IDIF)}$ quantification denoting significant reduction in heterozygous (HET) mice compared to WT littermates. \*\**p*<0.01, \*\*\**p*<0.001, \*\*\*\**p*<0.0001.
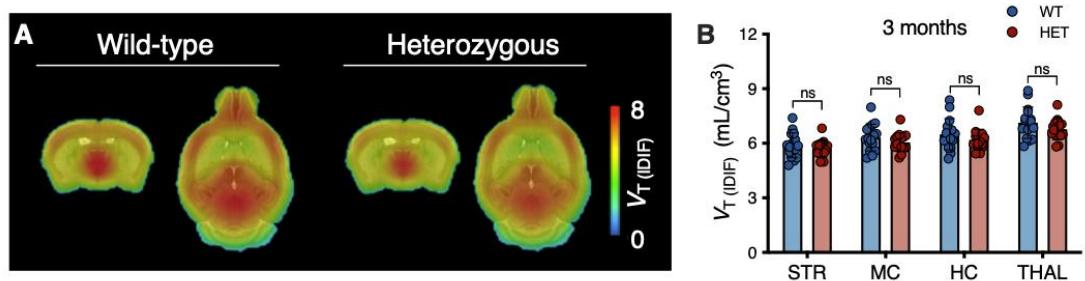
**FIGURE 2. $^{11}$C-UCB-J binding is not altered in pre-symptomatic heterozygous mice.**
(**A**) Mean parametric $^{11}$C-UCB-J $V_{T\ (IDIF)}$ maps of 3-month old mice overlaid on MRI template for anatomical localization. (**B**) Cerebral $V_{T\ (IDIF)}$ quantification at 3 months does not differ between genotypes. ns = non-significant.
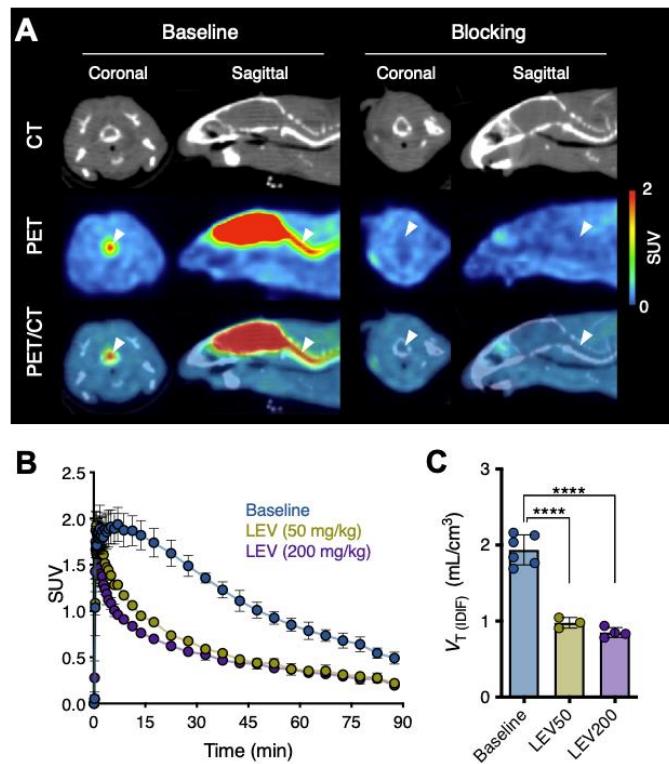
**FIGURE 3. $^{11}$C-UCB-J binding is specific and quantifiable in the mouse spinal cord**

(**A**) Representative $^{11}$C-UCB-J SUV PET/CT images of WT mouse during baseline and following pre-treatment with levetiracetam (LEV, 200 mg/kg, i.p.). Arrowheads indicate the cervical spinal cord. (**B**) Cervical spinal cord SUV time-activity curves showing a dose-dependent blocking effect. (**C**) Quantification of $^{11}$C-UCB-J $V_{T \, (IDIF)}$ in the cervical spinal cord. ****$p<0.0001$.
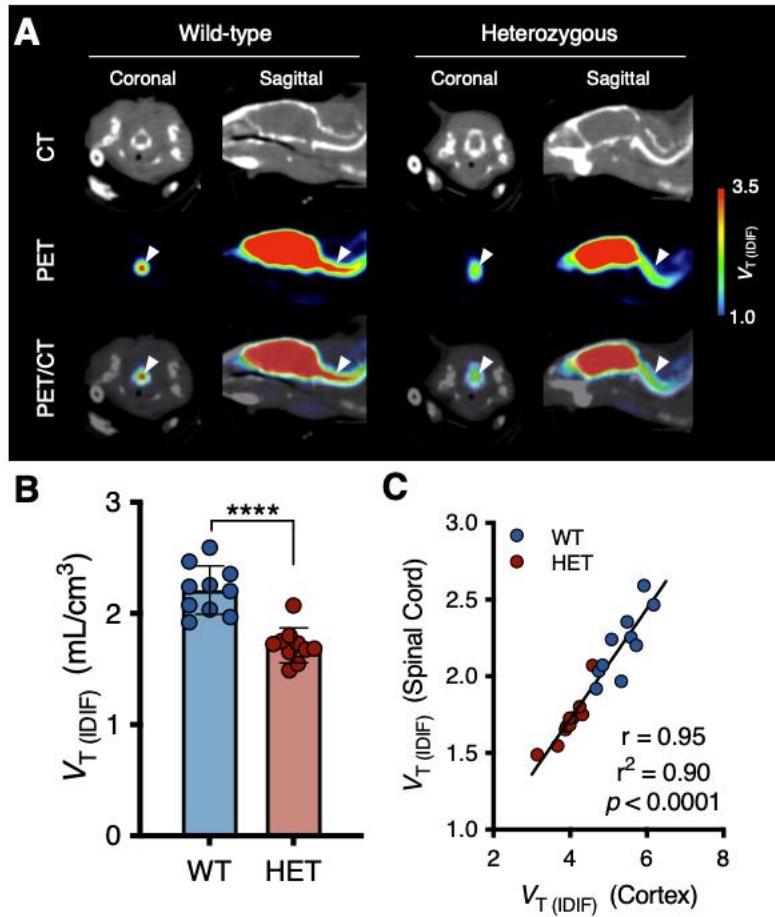
**FIGURE 4. ^{11}C-UCB-J binding is decreased in the spinal cord of symptomatic heterozygous mice.** (**A**) Representative maps of 16-month old mice overlaid on CT. Arrowheads indicate the cervical spinal cord. (**B**) Spinal $V_{T\,(IDIF)}$ is significantly lowered in 16-month old heterozygous (HET) mice compared to WT. ****$p<0.0001$. (**C**) Correlation between spinal and cortical ^{11}C-UCB-J binding.
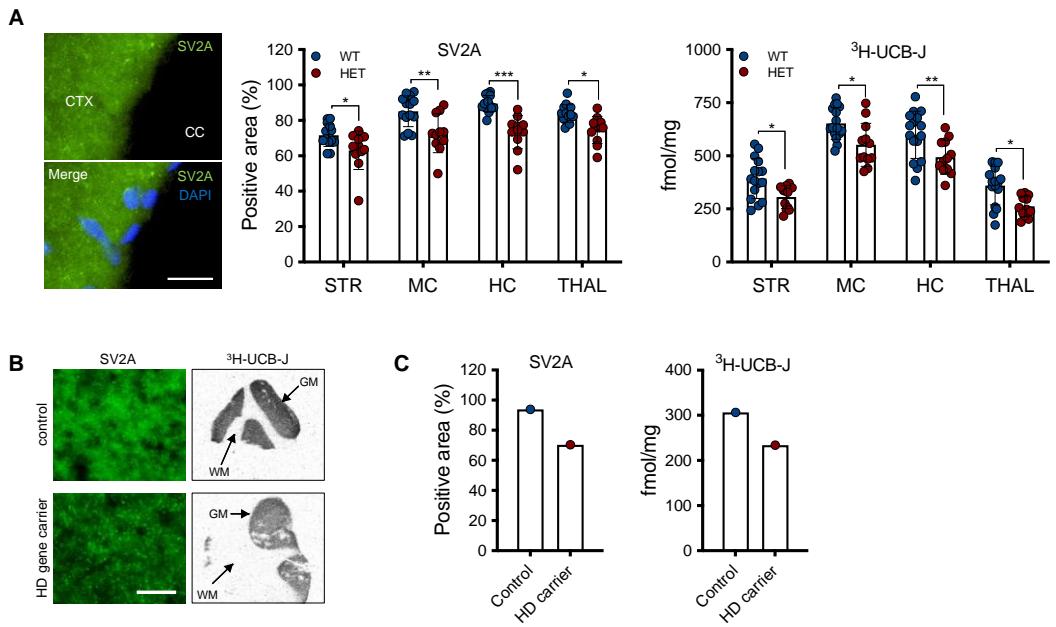
**FIGURE 5.** *Post-mortem* **quantification displayed SV2A reduction in HD**. (**A**) SV2A immunostaining and ^{3}H-UCB-J specific binding in the murine brain. (**B**) Representative SV2A immunostaining and ^{3}H-UCB-J total binding autoradiograms of human control and HD gene carrier. (**C**) ^{3}H-UCB-J specific binding and SV2A immunostaining tissue suggest a reduction in cortical SV2A in human tissue. $*p<0.05$, $**p<0.01$, $***p<0.001$. CTX = cortex, CC = corpus callosum. Scale bars = 20 µm.

# SUPPLEMENTAL INFORMATION

**SUPPLEMENTAL TABLE 1.** Scan parameters for ^{11}C-UCB-J PET imaging.

| Age (months) | Genotype | Sample size (n) | Molar activity (GBq/µmol) | Injected dose (MBq) | Injected mass (µg/kg) | Body weight (g) |
|---|---|---|---|---|---|---|
| 3 | WT | 16 | 77 (15.3) | 4.8 (1.0) | 1.31 (0.21) | 28.1 (2.8) |
| | HET | 16 | 77 (15.3) | 4.6 (0.9) | 1.28 (0.21) | 27.6 (1.8) |
| 7 | WT | 17 | 107 (40.3) | 5.9 (1.4) | 1.17 (0.22) | 31.1 (2.3) |
| | HET | 18 | 108 (36.7) | 5.8 (1.4) | 1.15 (0.15) | 29.8 (1.5) |
| 10 | WT | 15 | 102 (43.8) | 5.9 (1.5) | 1.07 (0.26) | 31.6 (1.8) |
| | HET | 16 | 111 (50.9) | 5.9 (1.5) | 1.07 (0.30) | 29.0 (1.7) |
| 16 | WT | 16 | 95 (2.9) | 5.9 (0.8) | 1.10 (0.20) | 32.0 (2.9) |
| | HET | 14 | 95 (10.9) | 4.8 (0.9) | 1.07 (0.21) | 26.1 (1.6) |

Values are expressed as mean (SD). WT = wild-type, HET = heterozygous.

**SUPPLEMENTAL TABLE 2.** Linear mixed-model statistical analysis of the longitudinal

[11]C-UCB-J $V_{T(IDIF)}$ PET study.

| Brain region | Genotype effect | | Time effect | | Genotype*Time effect | |
|---|---|---|---|---|---|---|
| | *F (DFn, DFd)* | *P* | *F (DFn, DFd)* | *P* | *F (DFn, DFd)* | *P* |
| Striatum | 32.53 (1,34) | < 0.0001 | 8.17 (2, 52) | 0.0008 | 1.73 (2, 52) | 0.1873 |
| Motor cortex | 33.39 (1,34) | < 0.0001 | 9.65 (2, 52) | 0.0003 | 3.01 (2, 52) | 0.0573 |
| Hippocampus | 39.83 (1,34) | < 0.0001 | 8.54 (2, 52) | 0.0006 | 2.59 (2, 52) | 0.0847 |
| Thalamus | 44.40 (1,34) | < 0.0001 | 7.94 (2, 52) | 0.0010 | 1.58 (2, 52) | 0.2153 |

28

**SUPPLEMENTAL TABLE 3.** ^{11}C-UCB-J $V_{T\,(IDIF)}$ values for WT and heterozygous animals imaged at each time point. The table includes Cohen's effect size (*d*) for each genotypic comparison.

| Age | Genotype | ^{11}C-UCB-J $V_{T\,(IDIF)}$ (mL/cm$^3$) | | | |
|-----|----------|----------|--------------|-------------|----------|
| | | Striatum | Motor Cortex | Hippocampus | Thalamus |
| 3M | WT | 5.89 (0.68) | 6.38 (0.82) | 6.49 (0.85) | 7.13 (0.86) |
| | HET | 5.68 (0.45) | 6.04 (0.50) | 6.18 (0.56) | 6.76 (0.56) |
| | | *d* = 0.36 | *d* = 0.50 | *d* = 0.43 | *d* = 0.51 |
| 7M | WT | 5.48 (0.62) | 5.86 (0.66) | 6.14 (0.67) | 6.67 (0.70) |
| | HET | 4.76 (0.68)** | 5.05 (0.76)*** | 5.35 (0.75)** | 5.68 (0.83)*** |
| | | *d* = 1.10 | *d* = 1.13 | *d* = 1.11 | *d* = 1.29 |
| 10M | WT | 5.21 (0.45) | 5.47 (0.44) | 5.84 (0.46) | 6.32 (0.55) |
| | HET | 4.68 (0.54)** | 4.91 (0.52)*** | 5.21 (0.53)** | 5.55 (0.62)*** |
| | | *d* =1.06 | *d* = 1.16 | *d* = 1.27 | *d* = 1.31 |
| 16M | WT | 5.13 (0.51) | 5.51 (0.57) | 5.79 (0.57) | 6.23 (0.63) |
| | HET | 4.10 (0.38)**** | 4.28 (0.45)**** | 4.52 (0.44)**** | 4.87 (0.49)**** |
| | | *d* = 2.29 | *d* = 2.39 | *d* = 2.49 | *d* = 2.41 |

Values are reported as mean (SD). WT = wild-type, HET = heterozygous, M = months.
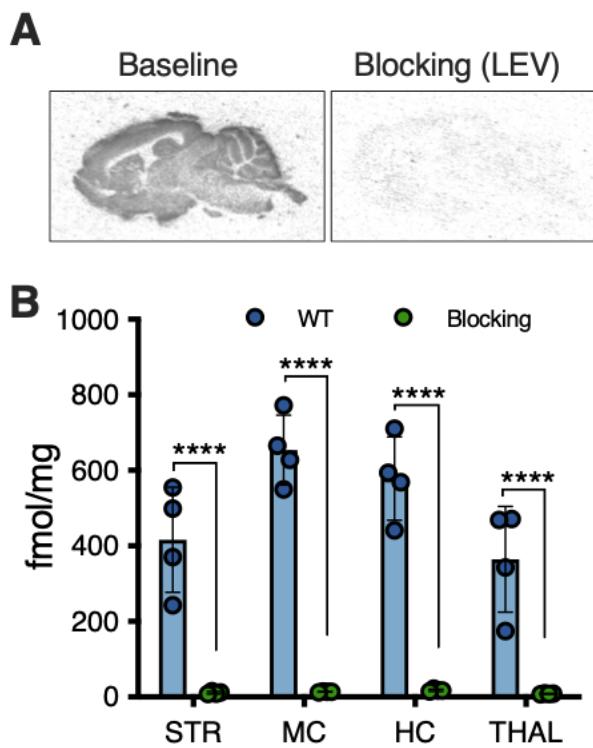
**SUPPLEMENTAL FIGURE 1.** (**A**) Representative total binding autoradiograms of $^3$H-UCB-J during with or without co-incubation with levetiracetam (LEV, 1 mM) in the same animal. (**B**) $^3$H-UCB-J specific binding during baseline and coincubation with LEV. $n = 4$. ****$p < 0.0001$. STR = striatum, MC = motor cortex, HC = hippocampus, and THAL = thalamus.
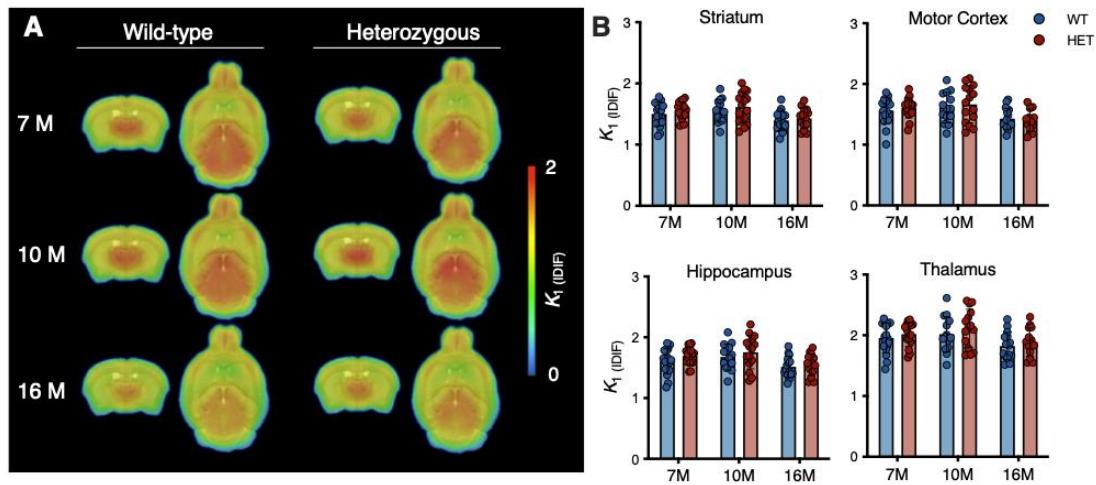
**SUPPLEMENTAL FIGURE 2. The decreased ^{11}C-UCB-J binding in** heterozygous **mice is not due to altered** $K_{1\ (IDIF)}$**.** (**A**) Mean $K_{1\ (IDIF)}$ maps overlaid on MRI template for anatomical localization. (**B**) Cerebral $K_{1\ (IDIF)}$ is not altered in heterozygous (HET) mice compared to WT littermates.

**GRAPHICAL ABSTRACT**

Huntington's Disease (HD)
mouse model
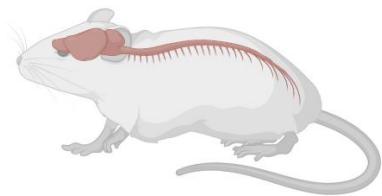
$^{11}$C-UCB-J  PET imaging



HD mice
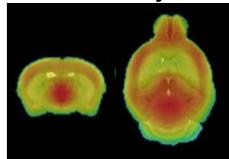
Healthy      Pre-symptomatic      Symptomatic